

RESONANT ORBITS AND THE HIGH VELOCITY PEAKS TOWARDS THE BULGE

MATTHEW MOLLOY

Kavli Institute for Astronomy & Astrophysics, Peking University,
Yi He Yuan Lu 5, Hai Dian Qu, Beijing 100871, China (matthewmolloy@gmail.com)

MARTIN C. SMITH

Key Laboratory for Research in Galaxies and Cosmology, Shanghai Astronomical Observatory,
Chinese Academy of Sciences, 80 Nandan Road, Shanghai 200030, China (msmith@shao.ac.cn)

N. WYN EVANS

Institute of Astronomy, Madingley Road, Cambridge, CB3 0HA, UK (nwe@ast.cam.ac.uk)

JUNTAI SHEN

Key Laboratory for Research in Galaxies and Cosmology, Shanghai Astronomical Observatory,
Chinese Academy of Sciences, 80 Nandan Road, Shanghai 200030, China (jshen@shao.ac.cn)

Draft Version 3; September 11, 2018

ABSTRACT

We extract the resonant orbits from an N-body bar that is a good representation of the Milky Way, using the method recently introduced by Molloy et al. (2015). By decomposing the bar into its constituent orbit families, we show that they are intimately connected to the boxy-peanut shape of the density. We highlight the imprint due solely to resonant orbits on the kinematic landscape towards the Galactic centre. The resonant orbits are shown to have distinct kinematic features and may be used to explain the cold velocity peak seen in the APOGEE commissioning data (Nidever et al. 2012). We show that high velocity peaks are a natural consequence of the motions of stars in the 2:1 orbit family and that stars on other higher order resonances can contribute to the peaks. The locations of the peaks vary with bar angle and, with the tacit assumption that the observed peaks are due to the 2:1 family, we find that the locations of the high velocity peaks correspond to bar angles in the range $10^\circ \lesssim \theta_{\text{bar}} \lesssim 25^\circ$. However, some important questions about the nature of the peaks remain, such as their apparent absence in other surveys of the Bulge and the deviations from symmetry between equivalent fields in the north and south. We show that the absence of a peak in surveys at higher latitudes is likely due to the combination of a less prominent peak and a lower number density of bar supporting orbits at these latitudes.

Subject headings: Galaxy: kinematics and dynamics — Galaxy: evolution

1. INTRODUCTION

It is now widely accepted that the Milky Way (MW) hosts a bar. Many methods have been used to map out the structure of the bar, such as IR photometry (Blitz & Spergel 1991; Dwek et al. 1995), gas dynamics (Englmaier & Gerhard 1999; Weiner & Sellwood 1999), star counts (López-Corredoira et al. 2007; Robin et al. 2012), microlensing (Udalski et al. 1994; Evans & Belokurov 2002; Wyrzykowski et al. 2015) and even the local kinematic landscape (Dehnen 1999, 2000). The MW bar exhibits a boxy-peanut shape (e.g., Dwek et al. 1995), which is host to an X-shaped structure that generates the “split” red clump (McWilliam & Zoccali 2010; Nataf et al. 2010; Saito et al. 2011; Li & Shen 2012; Ness et al. 2012). Significant observational effort has been expended in mapping the spatial density of the bar using the OGLE-III and VVV data (e.g., Wegg & Gerhard 2013; Cao et al. 2013). More recently, using a large sample of red clump giants, Wegg et al. (2015) derive a bar half-length of between ~ 4.5 and 5 kpc. However, uncertainties about the nature of the interface between the bar and the disk or spiral arms can strongly influence these estimates (Martinez-Valpuesta & Gerhard 2011). Uncertainty also surrounds some other fundamental parameters of the bar, such as the viewing angle θ_{bar} and the pattern speed of its rotation Ω_{bar} . The literature reports values for θ_{bar} in the range $\sim 20^\circ \lesssim \theta_{\text{bar}} \lesssim 45^\circ$ (e.g., Stanek et al. 1997; Benjamin et al. 2005) and for Ω_{bar}

in the range $\sim 25 \lesssim \Omega_{\text{bar}} \lesssim 50$ km s⁻¹ kpc⁻¹ (e.g., Antoja et al. 2014; Portail et al. 2015).

Despite a number of radial velocity surveys toward the Galactic bulge, kinematic substructure has rarely been observed. This is a pity, as such substructure may betray evidence of the processes that formed and shaped the bar. The Bulge RAdial Velocity Assay (BRAVA; Rich et al. 2007) and GIRAFFE Inner Bulge Survey (GIBS; Zoccali et al. 2014) both observed $\sim 10,000$ giants over a large region of the bulge, but revealed no signature of cold high velocity peaks. The ARGOS survey (see Ness & Freeman 2012; Ness et al. 2013) has also yet to reveal evidence for streams in the bulge, although their velocity distributions, cut according to metallicity, hint at the wealth of information contained in the kinematic data.

Recently, however, a cold high velocity peak has been observed by Nidever et al. (2012) in the Apache Point Observatory Galactic Evolution Experiment (APOGEE) commissioning data. For certain fields towards the Galactic Bulge, they find bimodal velocity distributions and identify cold ($\sigma \sim 20$ km s⁻¹) secondary peaks in the distribution of line of sight velocities at $v_{\text{los}} \sim 200$ km s⁻¹. The independent observations of Babusiaux et al. (2014) also hint at the presence of a high velocity peak, this time with red clump stars. The origin, and even the existence, of this feature has been the subject of recent debate (Li et al. 2014; Zoccali et al. 2014).

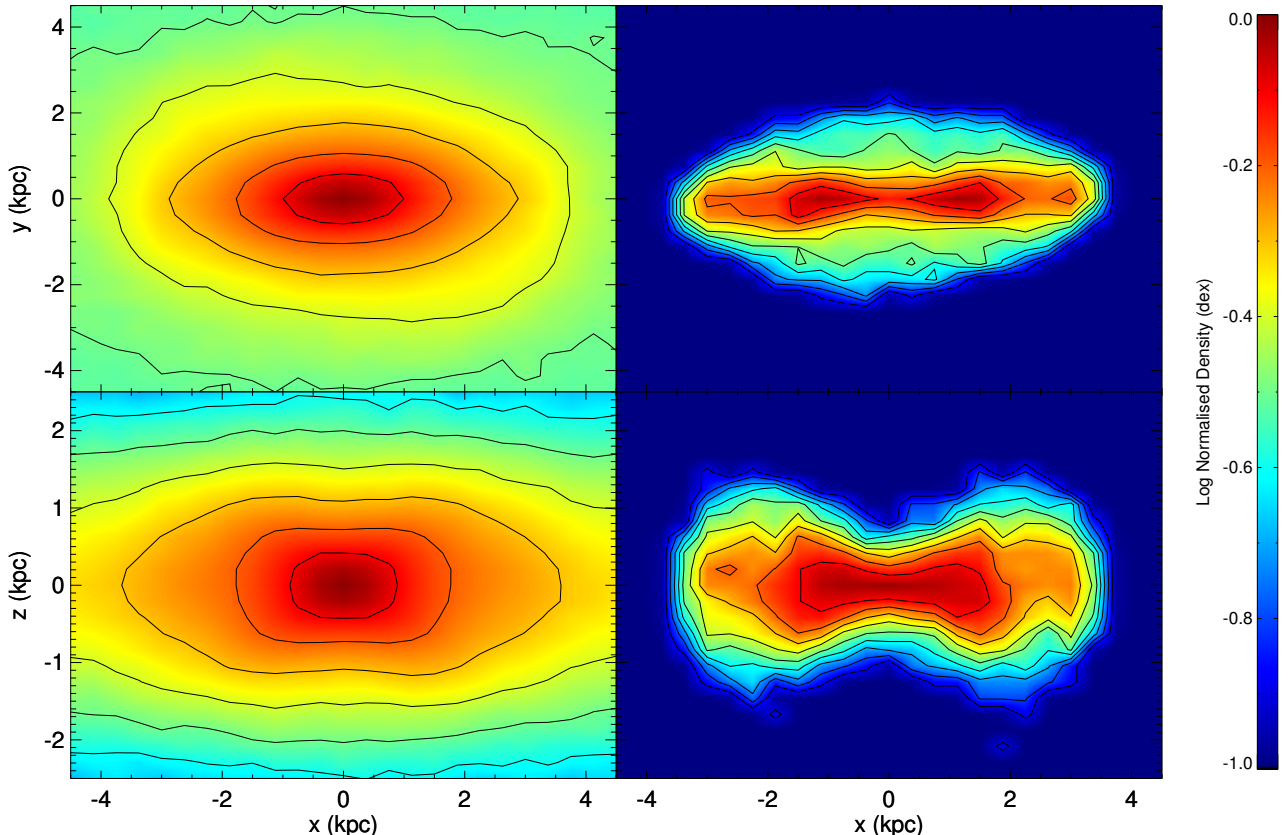


Figure 1. The normalised surface density (contours at 0.1 dex) in the x - y (top) and x - z (bottom) planes for all (left) and 2:1 resonant orbits (right).

Li et al. (2014) found the absence of a statistically significant cold high velocity peak in two N-body barred models. They also showed that it is possible for a spurious high velocity peak to appear if there are only a limited number of stars observed. Here, we look at the matter anew, using novel algorithms to extract nearly periodic orbits from bar simulations.

2. ORBITAL COMPONENTS IN THE BAR

In Molloy et al. (2015, hereafter M15), we introduced a method to identify resonant orbits in N-body simulations, and used it to provide a possible explanation for the bimodal velocity distributions observed towards the Galactic anti-Centre. The method is an alternative to identifying periodic orbits using frequency analysis and is well suited to analysis of evolving N-body models with a changing potential (see M15 for details). It is now applied to the inner parts of a barred disc model of the Milky Way. Here, a cold but thickened disc self-consistently develops a bar, which undergoes a buckling instability to form a Bulge that is a good match to that of the Milky Way (see Shen et al. 2010; Li & Shen 2012; Qin et al. 2015). Resonant orbits can be characterized by the fact that they close and return to a previously occupied location in phase space in some rotating frame. The method in M15 proceeds by recalculating the N-body orbits in many different rotating frames. We define a metric D_{ps} to measure the distance each particle travels from some arbitrarily chosen starting point in the rotating frame. If an orbit almost closes, D_{ps} should, at some point along its trajectory, be nearly zero. By defining a cut-off, we can extract a sample of the nearly closed orbits from the simulation. Resonant orbits can librate about each family’s parent orbit, so by defining tighter and tighter cuts on D_{ps} , we can extract cleaner and cleaner samples of resonant orbits. The choice of cut on D_{ps} is really set

by the problem in hand.

We make some minor modifications to the algorithm described in M15. In bars, there are always some chaotic orbits, especially near corotation. Indeed, chaotic orbits may make significant contributions to the structure and dynamics in barred systems. It has been shown that the fraction of chaotic orbits is sensitive to the bar strength and size (Manos & Athanassoula 2011; Manos & Machado 2014). Chaotic orbits may return arbitrarily close to their chosen starting point over long timescales (the Poincaré Recurrence Theorem), and can therefore be mistaken as periodic. Previously, we measured the phase space distance from a single point as the orbit proceeded on its trajectory over ~ 1 Gyr. Here, we define a time frame, unique to each particle, over which we apply the phase space distance method. For each particle, we measure the duration it takes to complete eight radial oscillations. This ensures that we have a long enough trajectory to extract high-order periodic orbits while excluding chaotic orbits that rapidly explore their phase space volume. For orbits very close to the centre, this time frame may be sampled by very few points so we interpolate the trajectory.

Also, instead of measuring the phase space distance from a single point, we find the time at which a particle reaches its first apocentre, t_0 . As we scan different rotating frames (between $37 \leq \Omega_p \leq 40$ km/s/kpc), we extract sections of the trajectories that lie in the range $\phi'(t_0)$ to $\phi'(t_0) + \pi/4$, where ϕ' is the azimuthal angle in the rotating frame. This gives us, say, n similar sections of the trajectory. If n is less than three, then we increase the duration over which we apply the method. The $n = 1$ section is the reference section which we compare to following test sections. The phase space distance D_{ps} is measured between successive points on the

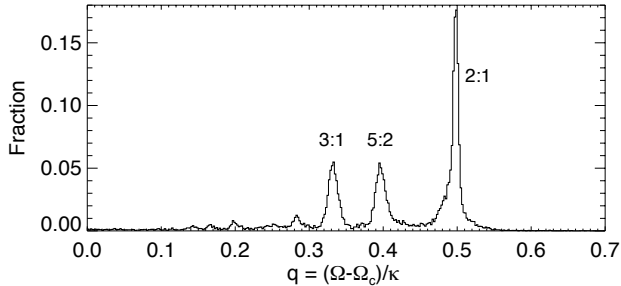


Figure 2. The distribution of $q = (\Omega - \Omega_c)/\kappa$ for the sample of periodic orbits with $R_g < 2.5$ kpc. We select 2:1 orbits as those with $0.48 \leq q \leq 0.52$, 3:1 orbits as those with $0.33 \leq q \leq 0.35$ and 5:2 orbits as those with $0.38 \leq q \leq 0.42$.

reference section and the test sections. We take the average D_{ps} between the orbit sections as a measure of how “closed” the orbit is - the lower the value, the more closed the orbit. Of the $n - 1$ D_{ps} values, we take the minimum and in the following we adopt a cut on the phase space distance of $D_{ps} < 0.06$ (Over the course of an orbit D_{ps} varies between $0 < D_{ps} < \sqrt{2}$, see M15).

By extracting a sample of resonant orbits in the central regions, we can deduce the contribution they make to the structure of the bar. Figure 1 shows the normalized surface density of the inner parts of the disc. In the left panels, we show the x - y (top) and x - z (bottom) surface density for all of the particles in the simulation. The bar extends to ~ 4 kpc or $R_{CR}/a \approx 1.125$ and has an axis ratio of $b/a \approx 0.5$. This is slightly less extended than the value of 0.35 found by OGLE (Rattenbury et al. 2007) but agrees well with the structure derived recently from a large sample RR Lyrae (Pietrukowicz et al. 2014). The x - z surface density exhibits a strong boxy-peanut shape characteristic of buckled bars. We extract the resonant 2:1 orbits by estimating the azimuthal (Ω) and epicyclic (κ) frequencies for our sample of closed orbits. For each orbit, we calculate $q = (\Omega - \Omega_p)/\kappa$, where Ω_p is the pattern speed of the frame in which the orbit closes, or reaches its lowest D_{ps} . We then extract the 2:1 orbits as those having $0.48 \leq q \leq 0.52$. The surface densities are shown in the right panels of Figure 1. It is clear that the 2:1 orbits generate the backbone of the bar. The buckling instability has a noticeable effect on this family of orbits, inducing a large vertical velocity dispersion for stars at the end of the bar. The contribution of the 2:1 family to the boxy and peanut shape is unmistakable.

Of course, other orbit families are present in the simulation. Figure 2 shows the distribution of q -values for particles with $R_g < 2.5$ kpc. The most prominent family are the 2:1 orbits but there is also a significant contribution from the 3:1 ($q \approx 0.33$) and 5:2 ($q \approx 0.4$) orbit families. The relative fractions for these families is approximately 2:1:1 (where we have taken the 3:1 orbits as those with $0.31 < q < 0.35$ and the 5:2 orbits as those with $0.38 < q < 0.42$). The relative fractions between the orbit families remains largely unchanged using different cuts on D_{ps} . However, the normalisation of the phase space distance (see M15) affects the elongated 2:1 orbit family differently compared to the more circular 3:1 and 5:2 orbits. Consequently, we refrain from making any strong conclusions based on the relative fractions of the extracted periodic orbits. In any case, we choose a cut on the phase space distance that allows us to sample the phase space of each family sufficiently. So, while the relative fractions of each family is uncertain, the shapes of the distribution functions are robust.

3. VELOCITY DISTRIBUTIONS

The photometry and star counts for this model have already been shown to be a good match to observations. Indeed, the

Table 1
Line-of-sight velocity distributions for each of the APOGEE commissioning fields (truncated). Table 1 is published in its entirety in the electronic edition of ApJ, a portion is shown here for guidance regarding its form and content.

(l,b) ($^{\circ}$)	θ_{bar}	All Peak ^a km s $^{-1}$	2:1 Peak ^b km s $^{-1}$
(10.0,-2.0)	10 $^{\circ}$	60.2	192.9
	15 $^{\circ}$	55.2	192.4
	20 $^{\circ}$	56.3	175.6
	25 $^{\circ}$	51.9	180.9
(10.0,2.0)	10 $^{\circ}$	70.1	197.3
	15 $^{\circ}$	64.7	193.9
	20 $^{\circ}$	62.5	197.7
	25 $^{\circ}$	56.3	183.9

^a χ^2 fits to all particles in the field.

^b Maximum peak of 3-Gaussian fit.

simulation was tailored to match the kinematics towards the Galactic Bulge as seen by the BRAVA data (Shen et al. 2010). The pattern speed of the simulation bar stays roughly constant at ~ 40 km s $^{-1}$ kpc $^{-1}$ (see M15). This is in the middle of the range of values reported in the literature and is consistent with the most recent estimates from gas dynamics (Sormani et al. 2015)¹. A suite of simulations spanning the parameter space of bar size, strength, viewing angle and pattern speed is required to fully investigate their effect on the v_{los} distributions.

Since we can deconstruct the bar into its different orbital families, we can now characterize the contribution of each family to the velocity distributions. The APOGEE commissioning data revealed cold high velocity peaks for a number of Bulge fields. Binney et al. (1991) were the first to link the motions of gas towards the Bulge to orbits in (planar) elliptical potentials. Below, we will show that these peaks arise naturally as a result of the motions of resonant bar orbits, in particular, the 2:1 orbital family. Note that if we include all simulation particles in our v_{los} distributions we recover the results of Li et al. (2014), in which no cold peaks are found.

To generate mock v_{los} distributions, we first fix some fundamental parameters. We choose the Solar radius as $R_0 = 8.5$ kpc and the circular velocity at R_0 as $v_c = 220$ km s $^{-1}$. Varying these between reasonable values has only minor effects on the distributions. We assume an angle between the long axis of the bar and the Solar-Galactic Centre (GC) line of $\theta_{\text{bar}} = 15^{\circ}$ (we later justify the choice, where we explore a range of bar angles). We also limit the distances of the particles to between 3 kpc and 9 kpc and, in order to increase the numbers in the samples, we include particles from equivalent positions on either side of the disc and increase the diameter of the field by a factor of two compared to the APOGEE fields. As a further measure to increase the number of particles, we also average over 10 timesteps, making sure to take into account the (small) change in bar angle between timesteps.

The top panel of Figure 3 shows the kinematic data on the APOGEE commissioning fields of Nidever et al. (2012), together with their two Gaussian decomposition. In the bottom plot of Figure 3, we show the velocity distributions for our sample of 2:1 orbits. To avoid forcing fits to binned data, we instead opt for a more general approach. We populate Gaussian mixture models (GMMs) using a genetic algorithm that converges on probability distribution functions that could have produced the data². This only requires one to input the range of parameter space to explore. In order

¹Aumer & Schönrich (2015) have recently shown that the v_{los} distributions are only weakly affected by the pattern speed, at least between 25 and 30 km s $^{-1}$ kpc $^{-1}$.

²We do this using the freely available SOLBER routines: <http://www.ast.cam.ac.uk/~vasily/solber/>

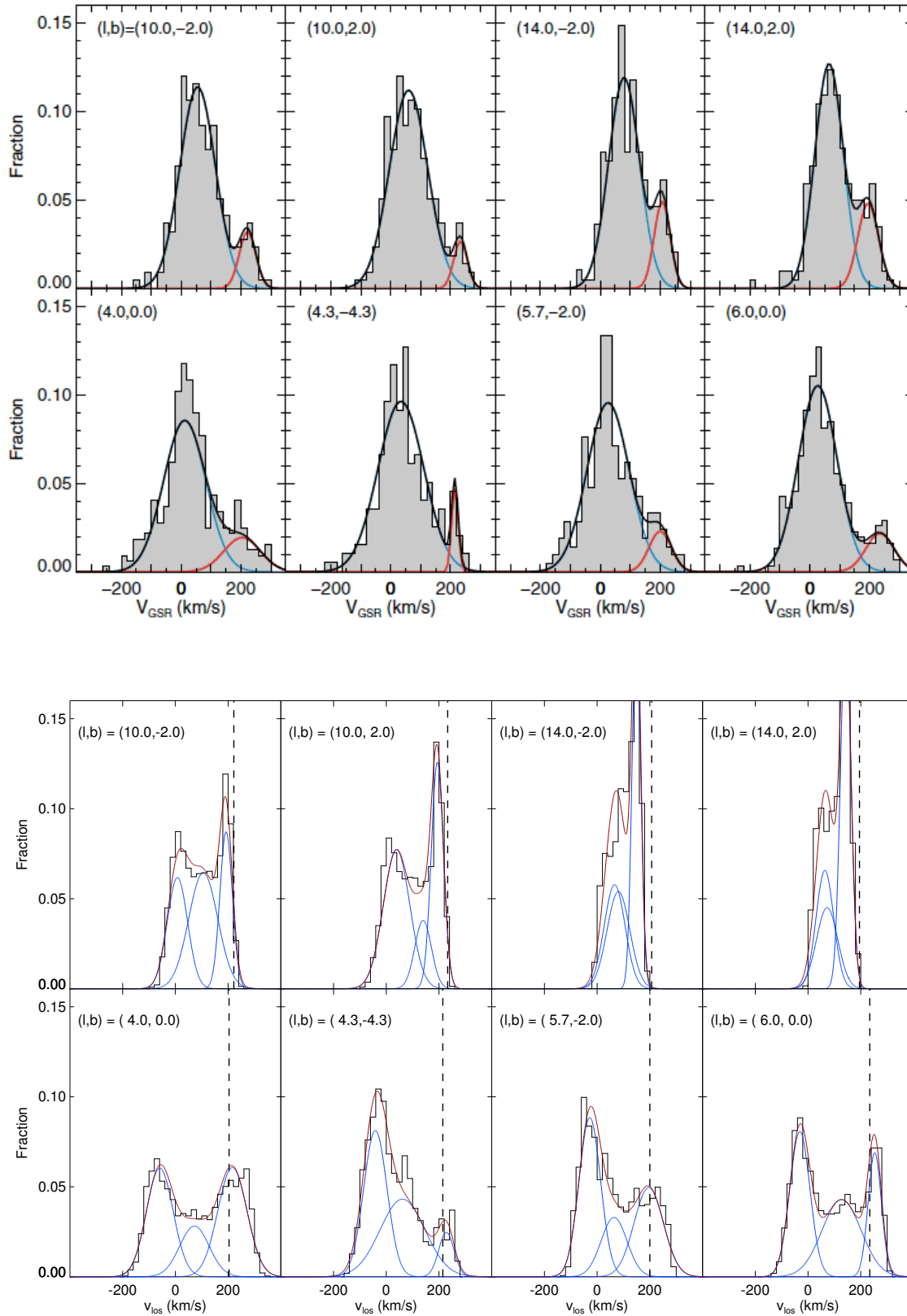


Figure 3. Top: For convenience, we show that v_{los} distributions from Nidever et al. (2012). The blue and red curves show their decomposition of the velocity histogram into two Gaussians. **Bottom:** The v_{los} distributions for 2:1 resonant orbits in each field, assuming a bar angle of 15° . A genetic algorithm has been used to populate a 3-Gaussian mixture model for the data. The underlying Gaussians are shown as blue curves and the locations of the peaks reported in Nidever et al. (2012) as the vertical dashed lines. The positions of the peaks show the locations at which 2:1 resonant orbits make the largest contribution to the observed histograms, which of course also include contributions from other orbital families.

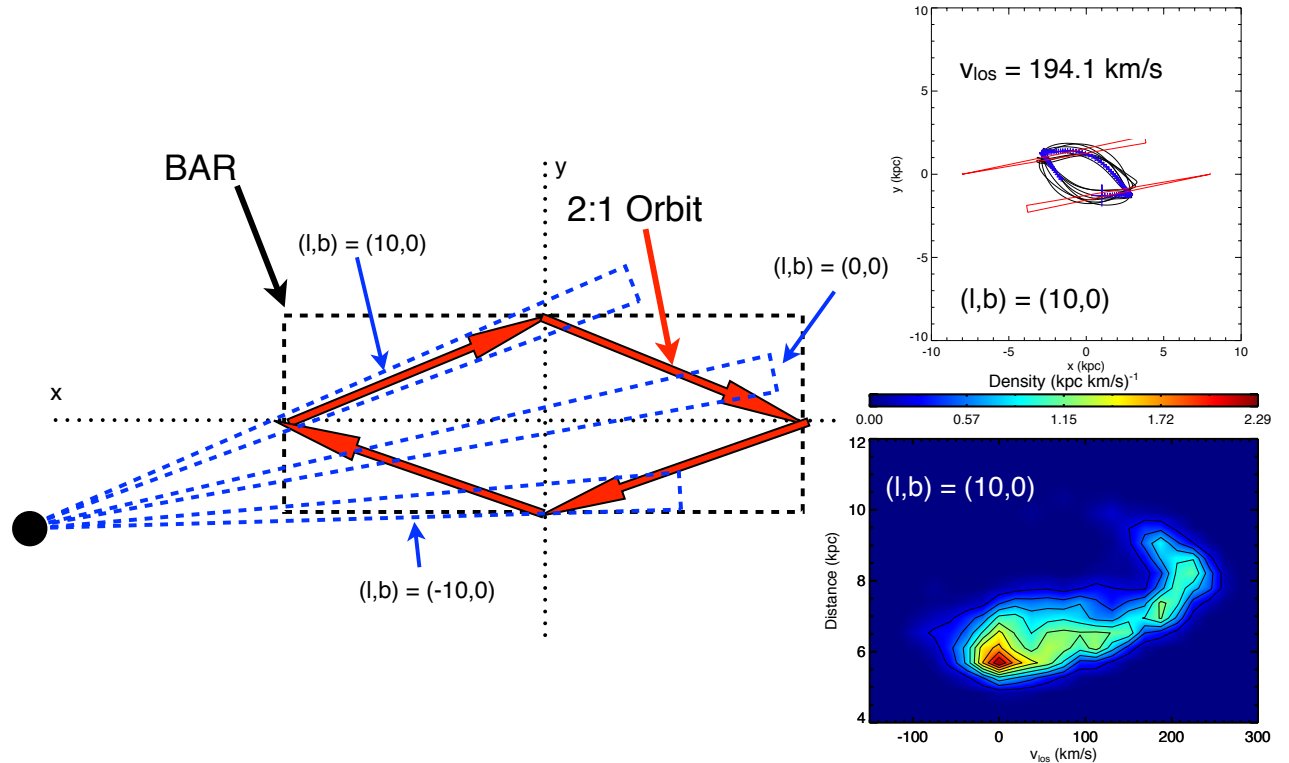


Figure 4. A schematic (and simplified) representation of a 2:1 bar orbit. The red arrows represent the motion of the particle in the frame of the bar (the black dashed box). For different fields, represented by the blue dashed lines, it is clear that this type of orbit gives different contributions to the line of sight velocities. For $l > 0^\circ$, we expect the star to be moving away, whilst the reverse is true for fields with $l < 0^\circ$. **Inset, top right:** A sample orbit from a high velocity peak at $(l, b) = (10, 0)$, the red triangles indicate the fields of view from which our sample is derived. The orbits are plotted over a period of ~ 1 Gyr with the final 100 timesteps indicated with blue crosses and the final timestep shown as the large blue cross lying inside the field of view. The line of sight velocity, assuming a Solar position of $(x, y) = (8.5, 0)$, is also listed. **Inset, bottom right:** The density of the 2:1 resonant orbits in the field at $(l, b) = (10, 0)$ as a function of v_{los} and distance. The highest velocity particles lie at a distance of ~ 8.5 kpc corresponding to pericentric passage. The lowest velocity particles lie at a distance of ~ 6 kpc corresponding to apocentric passage.

to compare the fits across each field, we force the distributions to be fit with three Gaussians. Initially, we fit each of the field's distributions with one to five Gaussians. We then performed likelihood ratio tests to see when adding an extra Gaussian component made no significant improvement. Most of the fields preferred either two (43.75%) or three (52.5%) Gaussians, while only a small proportion preferred one Gaussian (3.75%). Generally, the distributions are split into negative and positive velocity components, with an intermediate component in some fields. We interpret the negative velocity component as being due to particles on the near side of the bar, streaming towards apocentre. The high velocity component are then the particles streaming towards pericentre on the far side of the bar, while the intermediate component represents the particles that are slowing down as they approach apocentre, those at apocentre (with almost zero line-of-sight velocity) and those leaving apocentre, speeding up as they head towards pericentre. The shape, and number of components in the distribution is a non-trivial function of the field being observed, the chosen bar angle and the range of distances being sampled. For a selection of bar angles, we list the values of the peaks of the distributions for each field in Table 1. In the case of the three Gaussian fits to the 2:1 distributions, we list the highest valued peaks.

A crude representation of a 2:1 bar orbit is shown in Figure 4. The orbit, shown as the red arrows, reaches its apocentre at each end of the bar (on the x -axis), while the pericentres are located in the directions perpendicular to the bar (the black dashed box). The black dot represents the position of the Sun, so that the bar is rotating in a clockwise direction and the Galactic Centre-Solar position line is at an

angle close to 20° with respect to the bar. The dashed blue lines indicate the fields of view in Galactic coordinates. With $(l, b) = (10^\circ, 0^\circ)$, we can see how this type of orbit contributes to a high velocity component in this direction. For this line-of-sight, the measured v_{los} captures most of the components of Galactocentric v_R and v_ϕ and results in the high velocity peaks shown in Figure 3. In the Galactocentric frame, these stars have $v_R < 0 \text{ km s}^{-1}$ and $v_\phi \ll 0 \text{ km s}^{-1}$ which, for this particular direction in relation to the Solar position, make a significant contribution to v_{los} – in fact, almost all of the particle's velocity is coincident with the line of sight.

As a specific example, we take a sample orbit in the direction of $(l, b) = (10^\circ, 0^\circ)$ from the high velocity component ($v_{\text{los}} > 150 \text{ km s}^{-1}$) in the velocity distributions assuming a bar angle of 20° . We plot the orbit in the upper right panel of Figure 4 and indicate with the red lines the fields of view from which our sample is derived. The orbits are plotted over a period of ~ 1 Gyr with the final 100 timesteps indicated with blue crosses and the final timestep shown as the large blue cross lying inside the field of view. The line of sight velocity, assuming a Solar position of $(x, y) = (8.5, 0)$, is also listed.

A population of near-circular orbits would make a similar, but smaller, contribution to the high velocity peak in v_{los} since $v_R \approx 0 \text{ km s}^{-1}$. This direction also captures stars that are just reaching their maximum radius and so contribute to the negative velocity component in the distributions of v_{los} . The peaks of this component are at a lower velocity compared to the simple disc rotation model. This shows that resonant orbits in this direction imprint both low and high velocity kinematic signatures on the line of sight velocity distributions. A field centered on $(l, b) = (0^\circ, 0^\circ)$ passes through the

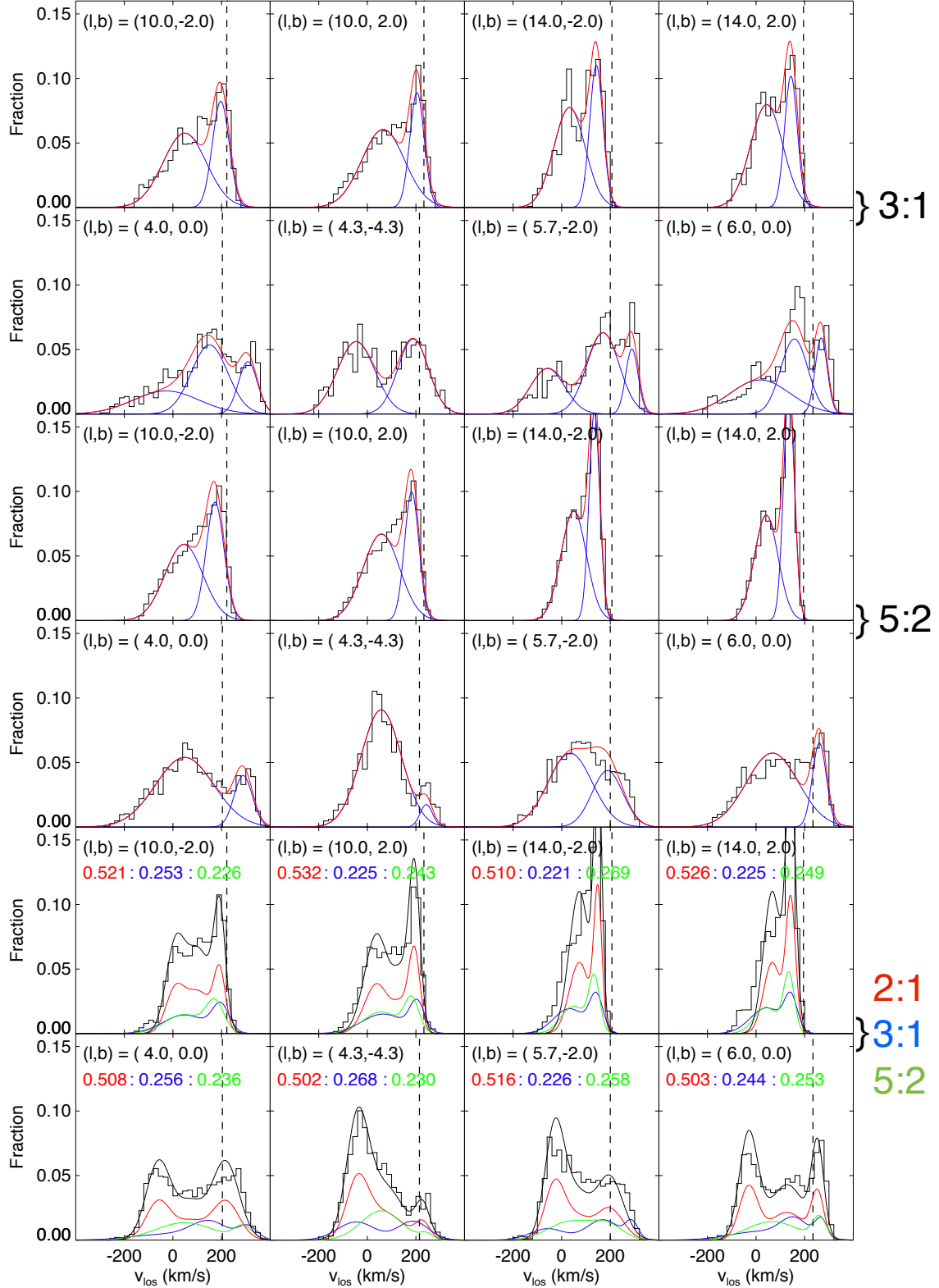


Figure 5. The v_{los} distributions for the 3:1 (top two rows) and 5:2 (middle two rows) orbit families in the APOGEE commissioning fields. For the 3:1 and 5:2 families we average over 35 & 50 timesteps (~ 0.34 & 0.48 Gyr) respectively to generate the distributions, which are then modeled with GMMs. The location of the observed peak for each field is indicated by the vertical dashed line (Nidever et al. 2012). The distributions due to the 2:1, 3:1 and 5:2 families combined are shown in the bottom two rows (where we have averaged over 10 timesteps or ~ 100 Myr). The relative fractions of each family are listed inset (2:1–red, 3:1–blue, 5:2–green). We overplot our simple model which uses relative fractions of 2:1:1 (for the 2:1, 3:1 and 5:2 families respectively) as the black curve. The components, using these relative fractions, are shown as the coloured curves where we use the 3 Gaussian fit to the 2:1 family from Figure 3 and the fits to the 3:1 and 5:2 families from the top four panels.

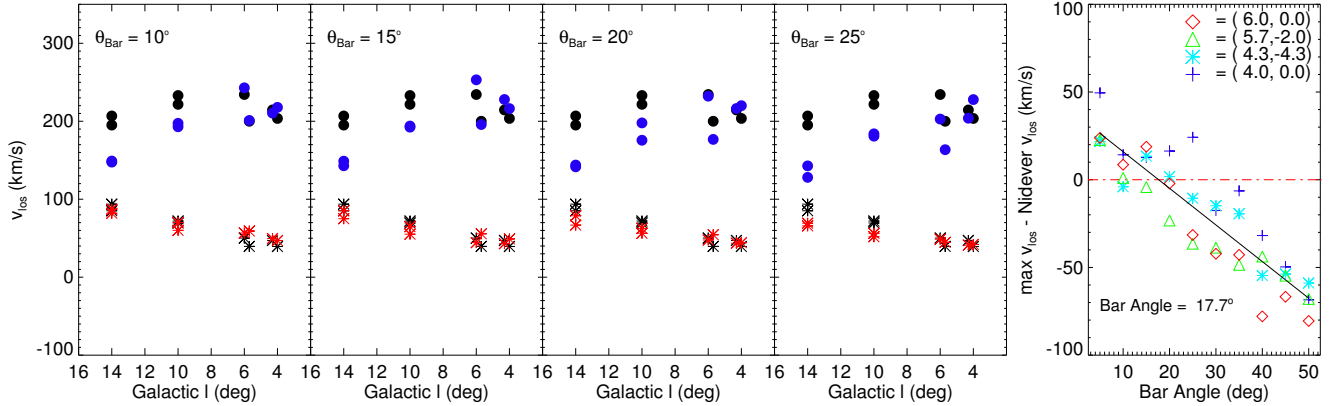


Figure 6. Left Panels: For the APOGEE commissioning fields shown in Nidever et al. (2012), we use Gaussian mixture models to characterize the v_{los} distributions assuming bar angles in the range $5^\circ \leq \theta_{\text{bar}} \leq 50^\circ$ (shown here is $10^\circ \leq \theta_{\text{bar}} \leq 25^\circ$). The black stars/dots represent the general/high velocity peaks seen in the APOGEE data (note that some longitudes have two points since APOGEE observed fields symmetric about the plane). The blue dots are the highest velocity peaks from our Gaussian mixture models for the 2:1 orbit velocity distributions. The red stars are the peaks from χ^2 fits to all particles in the fields. **Right Panel:** The difference in the values of the simulation and observed peaks for fields with $l < 10^\circ$ as a function of θ_{bar} , to which a linear fit is made (black line). The intersection of the fit to the 0 km/s difference suggests a bar angle of $\theta_{\text{bar}} = 17.7^\circ$.

whole structure of the bar and therefore catches stars with a negative v_{los} on the near side and with positive v_{los} on the far side. At negative l , the bar stars are approaching the Solar position and so imprint a high negative velocity component, mirroring the corresponding fields at positive l . Having a non-zero bar angle influences the differing shapes of the distributions between positive and negative longitude fields.

The lower right panel of Figure 4 shows the density of particles as a function of v_{los} and distance. For the line of sight $(l, b) = (10^\circ, 0^\circ)$, particles that are reaching apocentre contribute to the peak at $\sim 0 \text{ km s}^{-1}$ and are at smaller distances ($\sim 6 \text{ kpc}$). As the distance is increased, the particle’s velocity increases since both v_ϕ and v_R are increasing and also because the velocity vector is coincident with the line of sight. Of course this is only true for the 2:1 orbits, the wide range of other orbit families in static and evolving potentials will have more complicated morphologies (e.g., Pfenniger & Friedli 1991; Manos & Machado 2014). The highest velocity particles are approaching their pericentre occurring on the short axis of the bar at a distance of $\sim 8 \text{ kpc}$, very close to R_0 . This picture is consistent with our interpretation of the high velocity peaks in Bulge fields being due to the motions of resonant 2:1 bar orbits.

The other orbit families are also likely to have an influence on the v_{los} distributions. We see from Figure 2 that the 3:1 and 5:1 families make up a significant portion of our periodic orbits. If we plot the v_{los} distributions for these orbits it is clear that they are rich in structure (Figure 5). To account for their lower numbers, we average over 35 and 50 timesteps (336 Myr and 480 Myr) for the 3:1 and 5:2 families respectively. In this way, each of the chosen particles moves around their respective orbit pattern roughly twice. For fields with $l \geq 10^\circ$ the 3:1 (top two rows) and 5:2 (middle two rows) families also generate strong high velocity peaks (as before, we use a likelihood calculation to choose the number of Gaussian components). Just as for the 2:1 families, the peaks in these fields lie at a lower velocity compared to the peaks identified by Nidever et al. (2012) (vertical dashed lines). At lower longitudes ($l \leq 6^\circ$) these families also generate peaks coincident with the peaks identified in the data (e.g., 3:1 and 5:2 at $(l, b) = (5.7^\circ, -2.0^\circ)$). However, there are fields in which the peaks fail to match the data (e.g., 3:1 and 5:2 at $(l, b) = (4.0^\circ, 0.0^\circ)$). For certain bar angles θ_{bar} the 2:1 family can simultaneously, across a number of fields, generate peaks that are a good match to the data.

The relative fractions of each orbit family is an important factor in shaping the v_{los} distributions (i.e., the locations of

cold peaks). It is likely the case that the relative fraction in each field differs from the “global” fraction for the bulge as a whole. This is because each family has a distinct spatial density distribution. For example, the 2:1 family stays close to the long axis of the bar while the other families generally travel farther along the short axis. This, together with the uncertain distances probed in the APOGEE fields, makes it very difficult to derive the relative fractions from the data. We show the v_{los} distributions imprinted by the 2:1, 3:1 and 5:2 families combined in the bottom two rows of Figure 5. The combined 2:1, 3:1 and 5:2 v_{los} distributions average over 10 timesteps. As a fiducial model we apply simple relative fractions to the fits for each family (2:1:1 for the 2:1, 3:1 and 5:2 families respectively; for the 2:1 family we use the 3-Gaussian fits from the previous section) and overplot the simple model on the v_{los} distributions. The actual fractions from the model, listed in each panel, vary only slightly from field to field but for this exercise we have applied a uniform distance cut along each field. The distances probed in the data are likely to vary significantly with Galactic l and b . Given the small change in fractions between fields, it’s not surprising that the simple model matches the distributions quite well. With this model the high velocity peak is largely determined by the 2:1 family, especially for the fields with $b = 0^\circ$. At larger latitudes, the other families appear to make more significant contributions to the high velocity component, but never stronger than the 2:1 family.

With the tacit assumption that the locations of the peaks are set by the 2:1 family (i.e., that the relative fractions of the most populated families is close to 2:1:1, as above), can we use this insight to constrain the viewing angle of the bar, using the information on how the velocity peaks vary with Galactic position? In Figure 6 (left panels), the black stars and dots represent the locations of the peaks found by Nidever et al. (2012). Over-plotted as blue dots and red stars are the positions of the peaks from our models. Specifically, the blue dots are derived from the Gaussian mixture models for the 2:1 resonant orbits, whilst the red stars are extracted from χ^2 fits to all the particles in the field. It is clear that, although no single choice of viewing angle reproduces all the data, the trends in the velocity peaks are well-reproduced for bar angles $\sim 15^\circ$.

The fields with the largest deviations are the ones with the highest longitude, for which our simple picture probably breaks down. Although the peaks in these fields are quite pronounced, they systematically lie at lower values compared to the data. This could be due to one of two possible scenar-

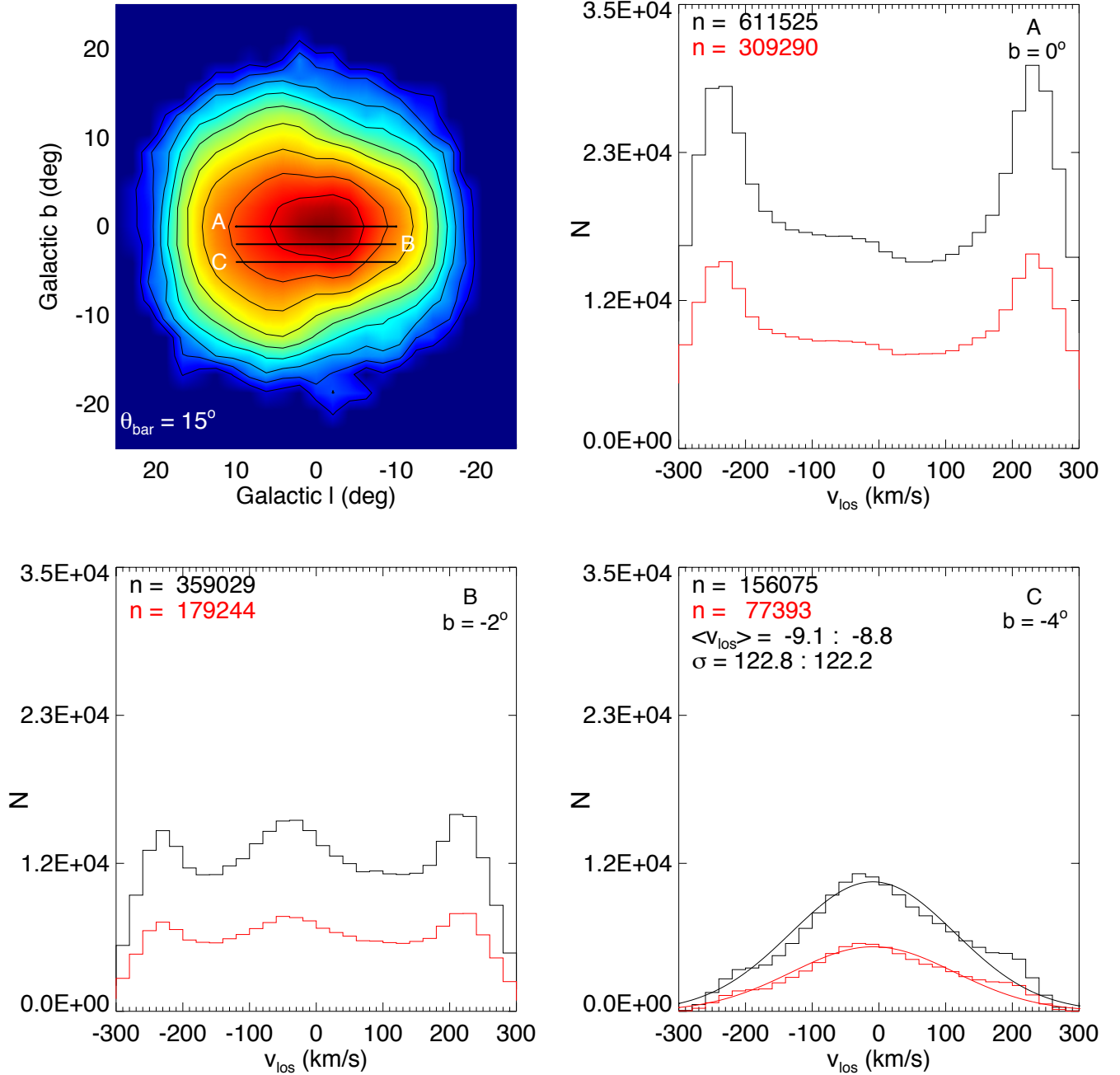


Figure 7. Top Left: The projected surface density of the 2:1 resonant orbits assuming a bar angle of $\theta_{\text{bar}} = 15^\circ$ (averaged over 0.48 Gyr). Horizontal lines indicate stripes in longitude from which the following histograms are drawn. **(A)** v_{los} distribution for the strip with $-10^\circ < l < 10^\circ$ and $b = 0^\circ$. The black histogram represents a strip of width $\Delta b = 1^\circ$ (thick) and the red, a strip of width $\Delta b = 0.5^\circ$ (thin). **(B)** As for panel A, but at $b = -2^\circ$. **(C)** As for panel A, but at $b = -4^\circ$. We also make χ^2 fits to the distributions, the mean and dispersion of which are listed for the thick and thin strips respectively.

ios. Firstly, being at high longitudes, particles in these fields feel a significant cumulative effect of the shallower potential. The high velocity particles in fields with $l \geq 10^\circ$ are at pericentre between 1.5 and 2.0 kpc along the short axis of the bar. We expect the potential to be somewhat shallower since the pure disc simulation is absent of a gaseous component and live halo that may relax into a more concentrated configuration after the formation of the bar. However, the simulation has been shown to be in good agreement with the kinematics observed by BRAVA (Shen et al. 2010), even as far out as $l = 10^\circ$. A good match is made to the mean velocities and

velocity dispersions, so that the comparison is made to the data through the whole line of sight. As we've shown above (Figure 4, bottom right), the high velocity peaks correspond to a limited range in distance. That the deviation from the observed peaks increases with l is another indication that a somewhat shallow potential is the cause.

Another possible scenario is that the peaks are in fact caused by another family of resonant orbits. We have checked the other major families in the bar, the 3:1 and 5:2 families. They do generate strong peaks in these fields but, as with the 2:1 orbits, the high velocity peaks are at systematically lower

values (combinations of the 2:1, 3:1 and 5:2 orbits also result in peaks with low values, see Figure 5). However, other higher order resonances may also be important in these regions. As mentioned in Nidever et al. (2012), the high velocity peaks are unlikely to be due to tidal streams. Although the Sagittarius stream lies close by on the plane of the sky, the high velocity stars show no preference for magnitude or metallicity and, in any case, the stream stars are not expected to appear in large numbers (Law & Majewski 2010).

Another way of synthesizing this information is presented in the right panel of Figure 6, which shows how the difference between the observed and simulation high velocity peak varies with assumed viewing angle of the bar. The observational data for each field are represented by the horizontal red dot-dashed line (i.e., the zero-difference line), and suggest viewing angles between 10° and 25° . Some scatter is expected, as the N-body model does not exactly reproduce the three-dimensional density of the inner Galaxy and the kinematical properties are subject to numerical shot noise.

4. DISCUSSION

We have shown that the high velocity peaks seen in the APOGEE commissioning data may be explained by the presence of a large family of 2:1 resonant orbits in the Galactic bar, as was tentatively suggested by Nidever et al. (2012). These orbits are elongated along the bar’s major axis, and must support the distended shape of the bar to provide its backbone. Indeed, it has already been shown by Binney et al. (1991) that the motion of gas towards the Bulge follows naturally from orbits in (planar) ellipsoidal potentials. When viewed at bar angles in the range $10^\circ < \theta_{\text{bar}} < 25^\circ$, the 2:1 orbits naturally give rise to secondary peaks in the line of sight velocity distributions at $v_{\text{los}} \sim 200 \text{ km s}^{-1}$. We have provided a pictorial explanation of this phenomenon.

Our interpretation is open to the objection that the method is not fully self-consistent. We have shown that the population of 2:1 orbits can generate the kinematic features to explain the data of Nidever et al. (2012), but we have allowed the normalization of the density in these orbits to vary independently of the N-body model from which they were extracted. This though is unlikely to be a serious concern, as the range of self-consistent equilibria for bars is wide and solutions will exist using different relative populations for the orbital families that comprise the bar. This has been demonstrated explicitly for the related problem of static triaxial ellipsoids (e.g., Statler 1987; Hunter 1995). For bars, the ability to exchange orbits without changing the density is indicated by both the non-unique decomposition into the classical and regular components found by Häfner et al. (2000) and the range of made-to-measure models reproducing the density inferred from the VVV survey (Wegg & Gerhard 2013) found by Portail et al. (2015). As we have mentioned above, the other resonant orbit families also produce rich structure in their velocity distributions. If we combine the 2:1, 3:1 and 5:2 orbits in our distributions, the high velocity peaks (which are somewhat more obscured) are dominated by the 2:1 orbits and so follow the trends outlined above to suggest $\theta_{\text{bar}} \approx 15^\circ$. Another important consideration is the range of distances probed by observations. Given the non-uniform distribution of dust towards the Galactic Bulge, it is certain that different fields are reaching different distances. Indeed the range of distances reached may vary significantly through just one field. The lower right panel of Figure 4 shows that the highest velocity 2:1 stars are placed at a distance close to R_0 . There is also likely to be some variation in the relative fractions of the different orbit families as one varies the distance probed. It is clear then that distance has an important role in shaping the velocity distributions.

4.1. Puzzles in the Data

Some issues remain about the high velocity peaks. The first is why symmetry is not seen between positive and negative latitude fields. Peaks are observed in the field at (4.3,-4.3) but not in the field at (4.3,4.3), the same goes for the fields

at (5.7,-2) and (5.7,2). The obvious explanation for such a difference is that the distances being probed differs between north and south. It is known that extinction in the north is greater than in the south (Gonzalez et al. 2012), which offers a possible explanation for the disparity. However, according to APOGEE estimates, although the average extinction is indeed greater for the field at (4.3,4.3) than for the field at (4.3,-4.3), the opposite is the case for the fields at (5.7,2) and (5.7,-2). The extinction data is at its most uncertain close to the plane of the disc, so it is unclear if this is causing the difference between symmetric fields. Another point to consider is that in the plane, where extinction is highest, strong peaks are seen. As we show below, a likely explanation here is that the number density of bar supporting orbits is higher in these regions.

The second major concern is the differences between different Bulge surveys. The BRAVA, ARGOS and GIBS surveys don’t report the detection of cold components in their v_{los} distributions. The presence of the peaks in the APOGEE data should be resolutely confirmed on analysis of the post-commissioning data. That the cold peaks are seen in one survey and not the others provides a possible clue as to the nature of bar supporting orbits. The clue lies in the different observing strategies and selection functions for the data. The color selections are similar, with each survey using cuts on $J - K$ color, but the magnitude ranges are not the same. These surveys each cover different footprints, with only APOGEE and GIBS observing a significant number of fields below $|b| = 4^\circ$. Most of our sample of resonant 2:1 orbits are confined close to the plane with $|b| < 5^\circ$ (corresponding to $\sim 0.75 \text{ kpc}$ at R_0). Figure 7 (top left) shows the projected surface density (on a log scale; contours at 0.1 dex) for the 2:1 family, where we have averaged over 0.48 Gyr. In the following panels we show the v_{los} distributions for stripes in longitude ($-10^\circ < l < 10^\circ$) centred on $b = 0^\circ, -2^\circ$ & -4° (A, B & C respectively; black histograms indicate a strip of width $\Delta b = 1^\circ$ and red, a strip of width $\Delta b = 0.5^\circ$). There is a stark difference between the distribution at $b = 0^\circ$ (A) and $b = -4^\circ$ (C). The strong peaks, clearly visible in the mid-plane, rapidly decrease in prominence as latitude is increased. At $b = -4^\circ$ there is only a small hint of a high velocity component at $\sim 200 \text{ km/s}$. This, along with the low density of 2:1 orbits, makes the detection of a cold peak much less likely at higher latitudes. It seems reasonable then that the BRAVA and ARGOS surveys don’t report the detection of cold peaks. This effect is unlikely to be the only important difference between the surveys. As we have shown above (Figure 4), the distances probed will also have a significant impact on the shape of the v_{los} distributions.

A more subtle difference is that the surveys observe different types of stars (GIBS & ARGOS: mainly red clump; APOGEE & BRAVA: mainly M-giants)¹. Since the targets that make up each survey differ in spatial (survey footprint, distance), temporal (ages) and chemical (color, magnitude) attributes, the question of why cold peaks are seen in one survey and not others is certainly challenging (it should also be noted that the observing strategy may be selecting stars with a low velocity dispersion, thereby thinning the overall distributions to reveal the cold peak). A better question might be whether APOGEE has stumbled on a selection strategy that preferentially selects bar stars, and if so, can the strategy be shown to be consistent with chemical and dynamical models of the Galactic Bulge?

We have so far not discussed in detail the effect of foreground or chaotic stars on the v_{los} distributions. Aumer & Schönrich (2015) suggest that the foreground stars play an important role in shaping the “main” distribution. The method outlined in M15 currently has no way of reliably identifying chaotic orbits but, in any case, they are unlikely to generate strong, long-lived features. Debattista et al. (2015)

¹It has been subsequently shown by Aumer & Schönrich (2015) that the APOGEE selection function is indeed selecting young stars.

have also recently suggested that substructure, similar to that seen in the APOGEE data, can be generated by a rotating nuclear disc. Their kpc-scale nuclear disc provides an alternative explanation for the observed kinematics.

So far, we have considered the cold peak to be a real and statistically significant feature. Li et al. (2014) showed that peaks can be generated by under-sampling the wings of a broad v_{los} distributions. It is unlikely however that similar features would be randomly drawn in a number of independent fields. Debattista et al. (2015) have also recently shown that such features are unlikely to arise due to Poisson noise.

5. CONCLUSIONS

We have set out a framework for understanding the substructure seen in the APOGEE data. As was suggested by Nidever et al. (2012), we have shown that the motions of stars along periodic bar orbits naturally give rise to cold peaks in v_{los} distributions. In particular, the 2:1 family are able to simultaneously generate peaks close to the observed values across a number of fields. This is a strong argument for the 2:1 family being the main driver behind the location of the peaks. Although uncertain, the relative fraction for the different families suggested by this simulation (and previous works, e.g., Sparke & Sellwood 1987) points to the 2:1 family being the most populous in barred potentials.

With this hypothesis in mind, we can constrain the viewing angle of the bar with the locations the peaks generated by the 2:1 orbits to be $10^\circ \lesssim \theta_{\text{bar}} \lesssim 25^\circ$. Although there remain uncertainties attached to this estimate, we are confident that large viewing angles can be discounted. The effect of fundamental bar parameters on the locations of the peaks remains to be explored in any detail. Uncertainties associated with the stellar distances, the effects of extinction and the selection function of the APOGEE survey make a complete comparison with models difficult. We have also shown, in agreement with Aumer & Schönrich (2015), that the higher order resonances can make a significant contribution to the v_{los} distributions, especially at high latitudes ($|b| > 2^\circ$). Close to the plane, however, the 2:1 family appears to play the dominant role and sets the locations of any high velocity peaks.

Finally, this work has demonstrated the power of the method introduced in Molloy et al. (2015) for extracting periodic orbits from N-body simulations in which the underlying gravitational potential is unsteady. By dissecting the bar into its constituent periodic families, we are able to study their characteristic kinematical and spatial signatures. Forthcoming wide field spectroscopic surveys of the Galactic centre are likely to discover further streams, kinematic features and substructure. We are confident that the techniques of the paper will have an important role to play.

The authors acknowledge financial support from the CAS One Hundred Talent Fund and NSFC Grants 11173002, 11333003, 11322326 and 11073037. This work was also supported by the following grants: the Gaia Research for European Astronomy Training (GREAT-ITN) Marie Curie network, funded through the European Union Seventh Framework Programme (FP7/2007-2013) under grant agreement no 264895; the Strategic Priority Research Program “The Emergence of Cosmological Structures” of the Chinese Academy of Sciences, Grant No. XDB09000000; and the National Key Basic Research Program of China 2014CB845700. This work made use of the super-computing facilities at Shanghai Astronomical Observatory.

REFERENCES

- Antoja, T., Helmi, A., Dehnen, W., et al. 2014, *A&A*, 563, A60
Aumer, M., & Schönrich, R. 2015, ArXiv e-prints, arXiv:1507.00907
Babusiaux, C., Katz, D., Hill, V., et al. 2014, *A&A*, 563, A15
Benjamin, R. A., Churchwell, E., Babler, B. L., et al. 2005, *ApJ*, 630, L149
Binney, J., Gerhard, O. E., Stark, A. A., Bally, J., & Uchida, K. I. 1991, *MNRAS*, 252, 210
Blitz, L., & Spergel, D. N. 1991, *ApJ*, 379, 631
Cao, L., Mao, S., Nataf, D., Rattenbury, N. J., & Gould, A. 2013, *MNRAS*, 434, 595
Debattista, V. P., Ness, M., Earp, S. W. F., & Cole, D. R. 2015, ArXiv e-prints, arXiv:1507.01433
Dehnen, W. 1999, *ApJ*, 524, L35
—. 2000, *AJ*, 119, 800
Dwek, E., Arendt, R. G., Hauser, M. G., et al. 1995, *ApJ*, 445, 716
Englmaier, P., & Gerhard, O. 1999, *MNRAS*, 304, 512
Evans, N. W., & Belokurov, V. 2002, *ApJ*, 567, L119
Gonzalez, O. A., Rejkuba, M., Zoccali, M., et al. 2012, *A&A*, 543, A13
Häfner, R., Evans, N. W., Dehnen, W., & Binney, J. 2000, *MNRAS*, 314, 433
Hunter, C. 1995, in *Annals of the New York Academy of Sciences*, Vol. 751, Three-Dimensional Systems, ed. H. E. Kandrup, S. T. Gottesman, & J. R. Ipser, 76
Law, D. R., & Majewski, S. R. 2010, *ApJ*, 714, 229
Li, Z.-Y., & Shen, J. 2012, *ApJ*, 757, L7
Li, Z.-Y., Shen, J., Rich, R. M., Kunder, A., & Mao, S. 2014, *ApJ*, 785, L17
López-Corredoira, M., Cabrera-Lavers, A., Mahoney, T. J., et al. 2007, *AJ*, 133, 154
Manos, T., & Athanassoula, E. 2011, *MNRAS*, 415, 629
Manos, T., & Machado, R. E. G. 2014, *MNRAS*, 438, 2201
Martinez-Valpuesta, I., & Gerhard, O. 2011, *ApJ*, 734, L20
McWilliam, A., & Zoccali, M. 2010, *ApJ*, 724, 1491
Molloy, M., Smith, M. C., Shen, J., & Wyn Evans, N. 2015, *ApJ*, 804, 80
Nataf, D. M., Udalski, A., Gould, A., Fouqué, P., & Stanek, K. Z. 2010, *ApJ*, 721, L28
Ness, M., & Freeman, K. 2012, in *European Physical Journal Web of Conferences*, Vol. 19, European Physical Journal Web of Conferences, 6003
Ness, M., Freeman, K., Athanassoula, E., et al. 2012, *ApJ*, 756, 22
—. 2013, *MNRAS*, 432, 2092
Nidever, D. L., Zasowski, G., Majewski, S. R., et al. 2012, *ApJ*, 755, L25
Pfnügner, D., & Friedli, D. 1991, *A&A*, 252, 75
Pietrukowicz, P., Kozłowski, S., Skowron, J., et al. 2014, ArXiv e-prints, arXiv:1412.4121
Portail, M., Wegg, C., Gerhard, O., & Martinez-Valpuesta, I. 2015, *MNRAS*, 448, 713
Qin, Y., Shen, J., Li, Z.-Y., et al. 2015, *ApJ*, 808, 75
Rattenbury, N. J., Mao, S., Sumi, T., & Smith, M. C. 2007, *MNRAS*, 378, 1064
Rich, R. M., Reitzel, D. B., Howard, C. D., & Zhao, H. 2007, *ApJ*, 658, L29
Robin, A. C., Marshall, D. J., Schultheis, M., & Reylé, C. 2012, *A&A*, 538, A106
Saito, R. K., Zoccali, M., McWilliam, A., et al. 2011, *AJ*, 142, 76
Shen, J., Rich, R. M., Kormendy, J., et al. 2010, *ApJ*, 720, L72
Sormani, M. C., Binney, J., & Magorrian, J. 2015, arXiv:1507.03078
Sparke, L. S., & Sellwood, J. A. 1987, *MNRAS*, 225, 653
Stanek, K. Z., Udalski, A., Szymanski, M., et al. 1997, *ApJ*, 477, 163
Statler, T. S. 1987, *ApJ*, 321, 113
Udalski, A., Szymanski, M., Stanek, K. Z., et al. 1994, *Acta Astron.*, 44, 165
Wegg, C., & Gerhard, O. 2013, *MNRAS*, 435, 1874
Wegg, C., Gerhard, O., & Portail, M. 2015, *MNRAS*, 450, 4050
Weiner, B. J., & Sellwood, J. A. 1999, *ApJ*, 524, 112
Wyrzykowski, L., Rynkiewicz, A. E., Skowron, J., et al. 2015, *ApJS*, 216, 12
Zoccali, M., Gonzalez, O. A., Vasquez, S., et al. 2014, *A&A*, 562, A66